PCCP

Accepted Manuscript

Journal Name

ARTICLE

Irreversible structural change of a dry ionic liquid under nanoconfinement

L. Andres Jurado[b], Hojun Kim[c], Andrea Arcifa[a], Antonella Rossi[a,d], Cecilia Leal[c], Nicholas D. Spencer[a], Rosa M. Espinosa-Marzal*[a,]

Studies of 1-hexyl-3-methyl-imidazolium ethyl sulfate ([HMIM] EtSO$_4$) using an extended surface forces apparatus show, for the first time, an ordered structure within the nanoconfined ionic liquid (IL) between mica surfaces that extends up to ~$60 \, nm$ from the surface. Our measurements show the growth of this ordered IL-film upon successive nanoconfinements—the structural changes being irreversible upon removal of the confinement—and the response of the structure to shear. The compressibility of this system is lower than that typically measured for ILs, while creep takes place during shear, both findings supporting a *long-range* liquid-to-solid transition. AFM (sharp-tip) studies of [HMIM] EtSO$_4$ on mica only reveal ~2 surface IL-layers, with order extending only ~ 3 nm from the surface, indicating that confinement is required for the long-range IL-solidification to occur. WAXS studies of the bulk IL show a more pronounced ordered structure than is the case for [HMIM] with bis(trifluoro-methylsulfonyl)imide as anion, but no long-range order is detected, consistent with the results obtained with the sharp AFM tip. These are the first force measurements of nanoconfinement-induced *long-range* solidification of an IL.

Introduction

Ionic liquids (ILs) are organic salts with melting points below 100 ºC. They display high electrochemical and thermal stability, are non-flammable and non-volatile,[1-3] and can be designed to interact with specific chemical groups, making them attractive in many applications including self-assembly media,[4] lubrication[5-12] and electrolytes for energy-storage systems.[1] These promising applications require a fundamental understanding of the IL behavior at the solid-liquid interface, both unconfined and in nanoconfinement.

Structural information on the solid-IL interface has been obtained by X-ray reflectivity,[13] neutron reflectometry,[14] sum frequency vibrational spectroscopy,[15] X-ray photoelectron spectroscopy (XPS),[16-20] atomic force microscopy (AFM),[21-29] and the surface forces apparatus (SFA).[30-42] Using the latter approach, the normal-force-versus-separation profiles reveal film-thickness transitions, as either single layers of ions or ion pairs are collectively squeezed out of the confined region. The layered structure is most pronounced at the solid-IL interface, decaying with distance from the substrate surface and typically vanishing beyond ~3-7 layers. The layered structure is rationalized in terms of ion-substrate and ion-ion interactions (van der Waals, hydrogen bonding, π-π interactions, solvophobic, and Coulombic), ion shape, size and packing (see refs.[21, 25, 33, 35-39]). The substrate plays a significant role in determining this solid-

like structure. Multi-layer structures exhibiting solid-like behavior have been imaged at the mica-IL interface.[29] Results suggest that the substrate templates the structure of the solid-like phase, as the edges of the solid-like structure follow discrete angles of the substrate lattice structure. Force measurements on ILs confined between a silica colloid probe and an atomically smooth polarized Au(111) substrate show an increase in the number of layers with increasing applied potential. The range of the layered IL-film extends to ~$5 \, nm$ (from the surface) at the highest potential, and the force required to squeeze the IL layers out increases with greater interaction strengths between the IL and the substrate, which increases with increasing surface potential.[22, 23] Angle-Resolved XPS[17-19] shows the influence of the substrate on the molecular arrangement of the IL at the solid-liquid interface; the surface potential also influences the IL molecular structure, as shown by IR adsorption spectroscopy.[43]

These experimental studies have indicated the solid-like behavior of ILs at the solid interface or under nanoconfinement, as extending only a few nm from the IL-solid interface, i.e. a *short-range solid-like behavior*. MD simulations also show the liquid-to-solid transition of a surface-adsorbed monolayer.[44] Contrasting results have, however, been obtained when thin films of 1-butyl-3-methyl-imidazolium bis(trifluoro-methyl-sulfonyl)imide were deposited on various substrates via evaporation of dilute IL-methanol solutions.[27] A layered IL-film with

a thickness of *50 nm* was observed to form on both mica and silica, i.e. of a much *longer-range order* than previously reported. This discrepancy was attributed to structural differences between evaporatively deposited thin films and equilibrium adsorbed layers, as had been observed in early AFM investigations on surfactants.[45]

The phase-transition behavior of ILs is complex, owing to their complex molecular structure. Imidazolium ILs that are liquid at RT have a strong tendency to supercool into a glassy state.[46] This is the case for 1-ethyl-3-methyl-imidazolium ethylsulfate ([EMIM] $EtSO_4$), which exhibits a glass transition at -78.4ºC upon cooling.[47] 1-hexyl-3-methyl-imidazolium bis(trifluoromethyl-sulfonyl)imide ([HMIM] Ntf2) has a melting point at ~-1ºC.[48] Differences in the observed phase-transition behavior between similar cations have been attributed to the molecular flexibility of the paired anion.[49] ILs can also form thermotropic ionic liquid crystals (ILCs) upon cooling, and crystallize upon further lowering of the temperature.[50, 51,52] The ion-ion interactions typically stabilize lamellar mesophases.[51] 1-alkyl-3-methyl-imidazolium ILs ([Cnmim]), with long alkyl chains (typically n >12 carbons, where n is the number of carbons in the alkyl chain) may behave as an ILC for particular anions.[51] For example, for [Cnmim] Ntf2, no mesophase could be observed for n between 5 and 18.[53, 54] Alkylsulfate anions with long alkyl chains (n>10) form thermotropic ILCs with pyridinium cations.[55] However, it is noteworthy that nanoconfinement can modify the phase-transition behaviour, the glass-transition temperature, and the melting and crystallization points of ILs.[56]

Here we present both force measurements and wide-angle X-ray scattering (WAXS) data for dry [HMIM] $EtSO_4$. We show that nanoconfinement leads to a *long-range order* of this IL that extends out to 60 nm from the IL-mica interface and is irreversible. WAXS shows that the bulk structure of this IL is more ordered than that of the other selected imidazolium ILs at RT. The effect of the relative humidity (RH) has been demonstrated in previous studies for other ILs,[20, 30, 31] and we will show its influence on [HMIM] $EtSO_4$ in a separate publication.

Results

IL compression with the extended surface forces apparatus

The normal force (F) between two mica surfaces across [HMIM] $EtSO_4$ was measured as a function of the surface separation (D) by continuously purging the chamber of the extended surface forces apparatus (eSFA) with dry N_2 at constant temperature (22±0.1 ºC). The surfaces were approached and separated at constant speed (0.2 nm/s to 5 nm/s). The maximum load applied in our measurements was 5 mN, which corresponds to a F/R-value[57] of 250 mN/m, and a Hertzian stress of 10 MPa. As the substrate flattens above 10mN/m, this pressure is overestimated. Moreover, the F/R-values shown in following diagrams are also overestimated above ~10mN/m as they are calculated assuming that R remains constant. Our studies on mica compression and deformation show that the error in D is smaller than 1 nm at the applied maximum load, but mica de-

formation does not affect the measured size of the transitions.[58] The surfaces were separated to D~1 μm between consecutive approaches.

Figure 1a shows the measured force vs. separation (called force isotherm) for confined [HMIM] $EtSO_4$ during consecutive approaches (force-separation curves from 1st (f1) to 4th (f4)) at 0.2 nm/s in a N_2 atmosphere. The steps in the first force-separation curve (f1) result from molecular-density fluctuations in the film[57], i.e. the ions form layers under confinement (see the red arrows pointing at 7 Å and 1.2 nm film-thickness transitions). As the surfaces approach each other, an IL-layer (expected to be composed of cations and anions to retain electroneutrality) is squeezed out from the contact region—a phenomenon that we denote 'film-thickness transition'. No artefacts in the refractive index were measured during the transitions (Figure S1a in ESI).

Figure 1: a) Force isotherms between mica surfaces across [HMIM] $EtSO_4$ in dry N_2 atmosphere during the 1st to the 4th approaches (from left to right). Equilibrium was not achieve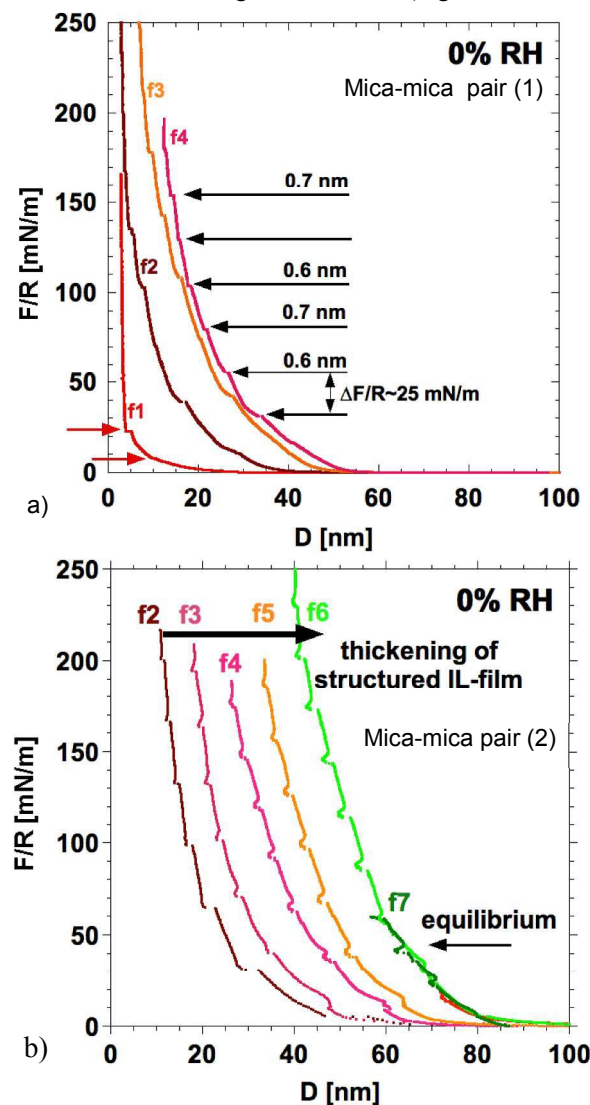d in this experiment. Constant approach of surfaces at 0.2 nm/s. b) Force isotherms between mica surfaces across [HMIM] $EtSO_4$ in dry N_2 atmosphere during the 2nd to the 7th approaches (from left to right) at 1 nm/s. The last two force measurements super-

pose, indicating that equilibrium has been achieved. The force isotherm f1 was not measured because the strong drift during equilibration brought the surfaces close to contact.

An increase in the onset (D) of the repulsive force, in the repulsion (F/R value), in the thickness of the structured film, and in the number of film-thickness transitions were observed in all measurements in dry N_2 upon successive approaches (f2 to f4 in figure 1a and, f2-f6 in figure 1b).

Moreover, the increase in force required for each further transition became approximately constant ($\Delta F/R \sim 25$ mN/m, in Figure 1a and ~ 28 mN/m in figure 1b), suggesting that the interaction between the IL layers at the slip plane was becoming gradually constant.

The force isotherms for another pair of mica surfaces in Figure 1b show that equilibrium was eventually reached after further approaches, the force-separation curves becoming superimposed (f6 and f7) and a hard-wall at D~42 nm being reached. These force-separation curves were measured at a faster approach speed (1 nm/s). These results are qualitatively similar to those obtained at 5 x lower speeds (Figure 1a) and at 5x higher speeds (not shown here). Increasing the time that the surfaces remained separated between consecutive approaches up to 12 h, and the distance to ~10 µm did not affect the described trends in the behaviour of the nanoconfined IL. This indicates that the qualitative change of the force isotherms upon consecutive confinement is influenced by neither speed nor by the total contact time.

It should be noted that the selected Y-axis is not logarithmic, as it was in our previous publications on ILs,[30, 31] in order to facilitate the identification of the film-thickness transitions superposed upon the much stronger repulsion, and to show the constant incremental force, $\Delta F/R$, required for each further transition. Owing to the stronger repulsion between the mica surfaces across [HMIM] EtSO$_4$ compared to all other investigated ILs, the load was increased to a maximum of 250 mN/m. The effect of a smaller applied compression on the evolution of the force isotherms is qualitatively similar, as shown in Figure S1b, but a more systematic study is currently underway.
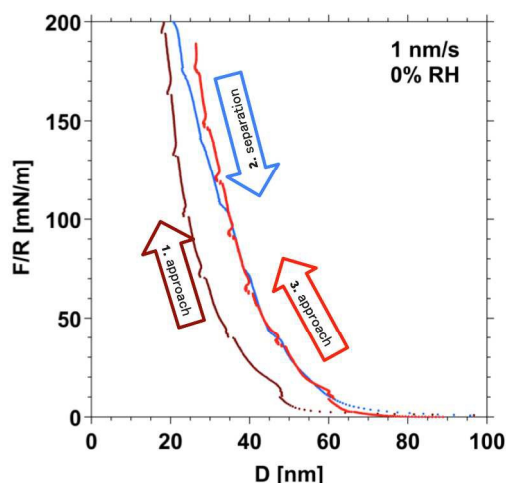
approach (3). The force isotherm during separation is superimposed upon the following force isotherm during approach, indicating that the IL-properties have changed irreversibly during compression. The surfaces were approached from and separated to ~ 1µm at constant speed of 1 nm/s.

The continuous growth (i.e. shift of the force curves to the right) of the solid-like IL-film is also reflected in an inverted hysteresis between force isotherms upon approach and separation (Figure 2). The force isotherm during separation is superimposed upon the force isotherm during the next approach, suggesting that an irreversible change of the IL structure occurs upon compression. If the solid-like IL that forms during approach remains at the contact upon separation, IL will flow in as the surfaces are separated and the resulting force-distance curve will lie above the force isotherm obtained upon approach. It cannot be excluded that the solid-like IL-film remains at the surface as the surfaces are separated to D~1 µm, i.e. as the nanoconfinement is removed, which is further supported by the AFM studies and will be discussed later.

It should be borne in mind that the force-separation curves for [HMIM] EtSO$_4$ shown in Figures 1 and 2 strongly differ from those measured under similar conditions for [EMIM] EtSO$_4$ (same anion)[31] and for [HMIM] with tris(pentafluoroethyl)-trifluorophosphate as anion (same cation).[30, 31] Furthermore, we have only found a qualitative agreement between experiments with different pairs of mica countersurfaces in [HMIM] EtSO$_4$, as shown in Figure 1, whereas we found a quantitative agreement for the experiments on other ILs. [24, 25]

The measured layer thicknesses as a function of the surface separation D (i.e. the IL-film thickness) are shown in Figure 3. Different symbols were used for different sets of mica surfaces. We found that the smallest film-thickness transitions are similar to those seen in measurements with other ILs. However, the layer thickness increases from 5 to 26 Å with D, its size exceeding that of the expected size of a single ion pair. This suggests the existence of stronger ion-ion correlations in [HMIM] EtSO$_4$ than in other investigated imidazolium ILs,[30, 31] leading to an enhanced layered structure, and solid-like behavior, upon nanoconfinement.

Figure 2: Force-distance curves for [HMIM] EtSO$_4$ confined between mica surfaces in dry N_2 atmosphere during approach and separation: approach (1), following separation (2), and final
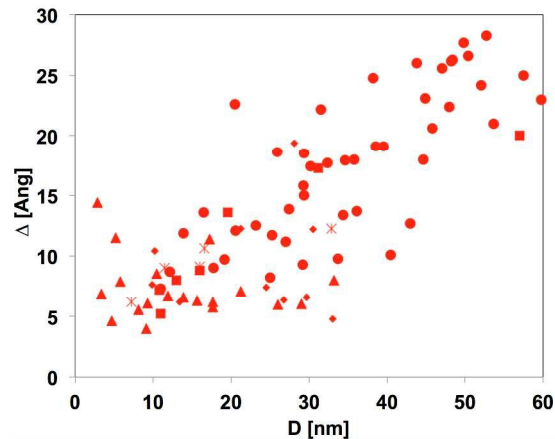

Figure 3: Size of film-thickness transitions Δ as a function of the IL-film thickness D in dry N_2. The thickness of the film transitions corresponds to the size of the layers of nanoconfined

[HMIM] EtSO$_4$. Different symbols were used for different sets of mica surfaces.

Time-dependent measurements of the surface separation, D(t), provide further information about the squeezing of IL-layers from the contact. Initially, the dynamics of layer squeezing is not different from that reported for other ILs[30]: as a layer of thickness Δ is squeezed out, the film thickness gradually decreases from D to D-Δ (Figure S2 in ESI). However, after consecutive approaches, the kinetics of the film-thickness transitions are completely different (Figure 4a): a sharp decrease of D indicates the rapid squeeze-out of IL layers, which is followed by a slow film dilation or expansion (slow increase in D with time). This dilation is responsible for an effective hard-wall effect, as the film thickness D remains approximately constant upon increase in load after squeezing-out and dilation. Figure S3 in ESI shows similar results for other pairs of mica surfaces. No change in the refractive index is observed during these characteristic transitions.

There are two possible explanations for the measured intriguing dilation after the squeezing out of a layer. Either the remaining IL ions between the surfaces rearrange such that the total film thickness increases, or else the ion pairs squeeze in as a result of stress relaxation. The former implies a decrease in density, which seems to contradict the observed strengthening of the film that is discussed later. Thus, we propose stress relaxation to cause the observed surface separation.
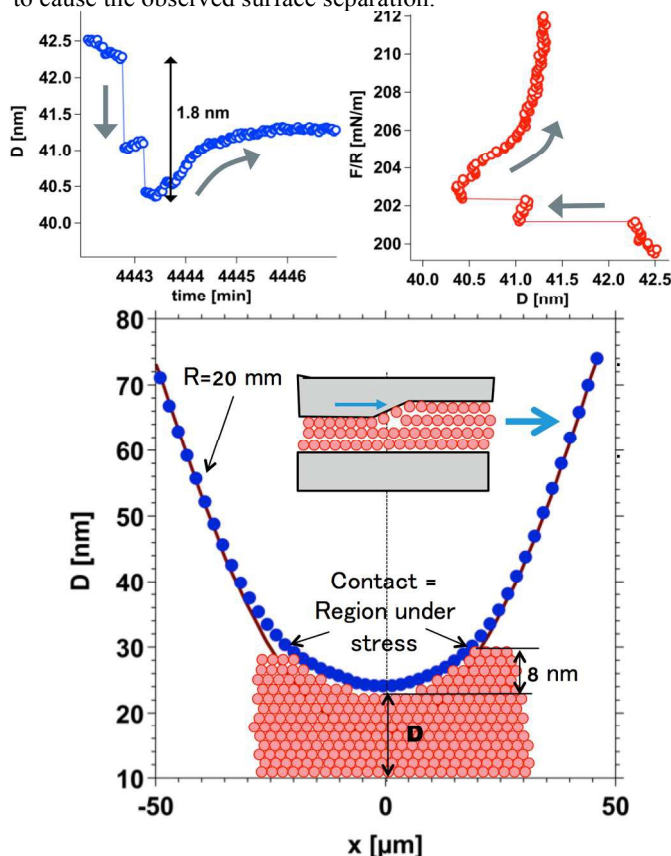

Figure 4: a) Time dependence of film-thickness transitions during transition and dilation: thickness D (Left) and normalized force F/R (Right). b) Measured 2D profile of the contact (dots) at maximum compression; the line shows the non-deformed (unstressed) contact, with a radius R=20 mm, and the flattened area with R'=30 mm.

It should be noted that D is measured at the point of closest approach (PCA), whereas the force includes contributions from the entire contact region.[57] The eSFA provides two-dimensional images of this region.[59] Figure 4b shows a cross-section of the *measured* mica contour at an applied load of 2.5 mN (dots). Owing to the curvature of the confining surfaces (note that models often assume the confinement region to be flat!), the number of layers is not the same within the loaded area. When layers are squeezed out, the confining surface needs to deform and conform (see inset). While the curvature decreases, the stress is distributed, the disjoining pressure decreases and as a result the surfaces slowly separate, and IL is squeezed in, leading most likely to the observed transition dynamics.

Colloidal-Probe AFM

Force isotherms for dry [HMIM] EtSO$_4$, repeatedly confined between a silica colloid probe with a 40 µm diameter and a freshly cleaved mica surface, are shown in Figures 5 and 6. In Figure 5, the 1st approach exhibits a short-range repulsion, similar to previously reported AFM measurements for other ILs[28] and is not further discussed here, while subsequent approaches (2nd and 3rd) show a gradual increase of repulsion onset. Due to the uncertainty of the absolute tip-substrate separation in AFM force measurements, we note that the abscissa is defined as an *arbitrary zero*. All force isotherms in the same diagram were offset to superpose the hard-walls, and therefore the repulsion onset indicates the distance from the hard-wall. It is, however, possible that the observed hard-wall effect occurs at a progressively increasing distance from the substrate upon repeated confinement, as in the SFA experiments.
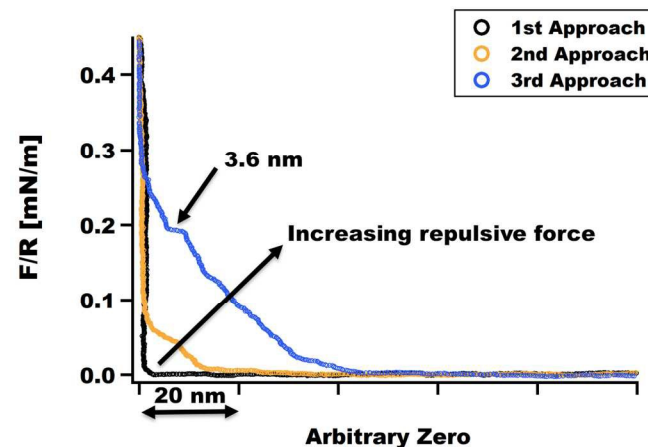
Figure 5: Force isotherms for dry [HMIM] EtSO$_4$ on mica acquired at the initial confinement position (1st, 2nd and 3rd approaches) in dry N$_2$ at constant speeds of 15, 17.5, and 20 nm/s respectively. The size of the most defined layer during the 3rd approach at 0.2 mN/m is 3.6 nm, which is also larger than the characteristic size of the layers measured for other ILs.[60] Hertzian contact pressures did not exceed 31 MPa.

The F/R-values obtained via AFM are of the same order of magnitude as those previously reported for other ILs (see e.g. ref.[60]), but they are much smaller than in SFA measurements[35, 37]. This large difference can be attributed to stronger collective

phenomena between the larger amount of trapped IL molecules in SFA measurements, as the confinement region is ~3 orders of magnitude larger than in the AFM measurements.[61, 62]

The film-thickness transitions superposed upon the force-separation curves in Figure 5 become more pronounced with repeated confinement, although they are much less defined than in SFA measurements, most likely owing to the much smaller confinement area.

A second set of force measurements were taken at a lateral off-set distance of ~ 50 μm from the initial confinement position, i.e. outside of the initial confinement region, and these are shown in Figure 6. The first approach already showed a *longer-range repulsion* with an onset at ~40 nm, which strongly differs from the results during the 1st approach in the initial confining position (Figure 5). Repeated approaches at the offset position confirm the increase in repulsion that eventually reaches equilibrium, as demonstrated by the relatively constant force – separation curve after the 5th approach. This was reproducible at other offset positions. The defined steps after the 5th approach are indicative of a more pronounced layered structure after repeated confinement. During the 5th and 7th approach, five and six film-thickness transitions or layers are resolved, respectively. The sizes of the layers typically increase with consecutive approaches. For example, at F/R~0.05 mN/m the step size for the 11th approach is approximately 6.6 nm, whereas the step sizes for the 5th and 7th approaches are approximately 2.6 and 4.1 nm, respectively. These results are qualitatively in agreement with SFA measurements, demonstrating that the induced *long-range structure* is not limited to the μm-size confining geometry in the SFA experiments.
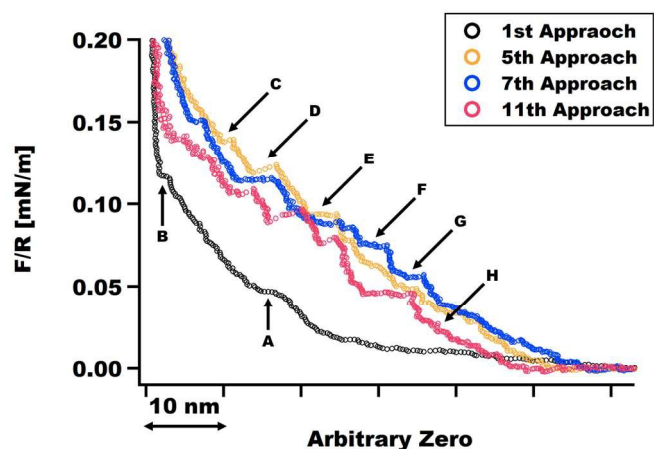
solid transition, as also indicated by the SFA experiments. To determine whether the colloidal sphere can transfer the solidi-fied IL, consecutive force measurements with the same colloidal sphere were performed on two separate pieces of mica to prevent the lateral propagation.

Figure 7 shows force isotherms for the first and second mica substrates. On the first piece of mica, a long-range repulsive force is already present on the first approach, which was observed in some experiments. Upon successive confinement, a gradual increase in the repulsive force and increasingly pronounced steps are observed. The 22nd approach has the largest observed push-through forces and layer sizes (5.3 nm and 5.1 nm at ~0.5 mN/m), again demonstrating the gradual increase in ordered structure in the nanoconfined IL-film.

On the second piece of freshly cleaved mica, the first approach (Figure 7) shows a seemingly *longer-range* repulsion with an onset at ~45 nm, which is more than twice the onset of repulsion during the 1st approach on the first piece of mica. Film-thickness transitions with sizes greater than the molecular diameter of the ion pair are superposed on the repulsive force, as indicated by the arrows. These results support the idea that solid-like IL can (at least partially) remain on the surface of the colloidal sphere as confinement is removed, and be transferred to other positions. However, these results do not completely exclude lateral propagation of the solid-like IL structure. These trends were reproducible across four replicate experiments with different pieces of mica and cantilevers. Thus, the results are in agreement with an irreversible liquid-to-solid transition of the nanoconfined IL.

Figure 6: Force isotherms for dry [HMIM] EtSO$_4$ on mica at an offset position during the 1st, 5th, 7th, and 11th approaches in dry N$_2$ at constant speeds of 20 (1st approach) and 15 (subsequent approaches) nm/s. The size of the IL-layers (A-H) is listed in Table 1 of the ESI.
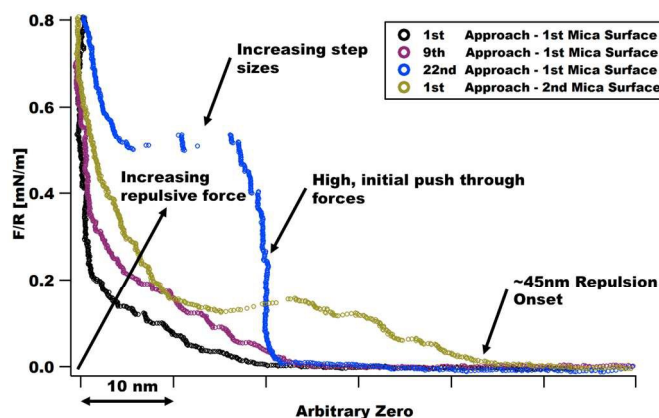
Figure 7: Force isotherms for a dry [HMIM] EtSO$_4$ film on the first mica substrate during the 1st, 9th, and 22nd approaches, and on the second dry IL on a separate mica substrate during the first approach. Isotherms were collected in a dry N$_2$ atmosphere at a constant speed of 10 nm/s. Hertzian contact pressures did not exceed 42 MPa.

The *long-range* repulsive force at the offset position suggests either a lateral propagation of the solid-like [HMIM] EtSO$_4$ from the initial confining position, or that the solid-like IL remains on the colloidal sphere and is transferred to the offset position. The latter suggests the irreversibility of the liquid-to-

Shear behaviour

The behaviour of dry [HMIM] EtSO$_4$ during shear was also investigated with the eSFA. The lower surface was mounted on a bimorph that laterally moves a fixed distance with time in a reciprocating fashion at constant speed (triangular waveform: see experimental methods for details). Figure 8a shows the lat-

eral force with time for a bimorph speed of 0.1 µm/s and two selected loads. The corresponding film thickness varies between 52 and 54 nm and therefore is much thicker than that of typical ILs in similar eSFA friction experiments (e.g. 1-2 nm in ref.[30, 34]). The increase in friction up to a yield point has been often observed previously in nanoconfined IL-films and has been attributed to *short-range* solid-like behavior.[34] After the onset of the slip at the yield point, no stick-slip was observed. Thus, either an inter-plane or wall slip[63] occurs. Considering the high surface charge of mica,[64] we suggest that an inter-plane slip is taking place.[65] During slip, we also observe an increase in the lateral force.
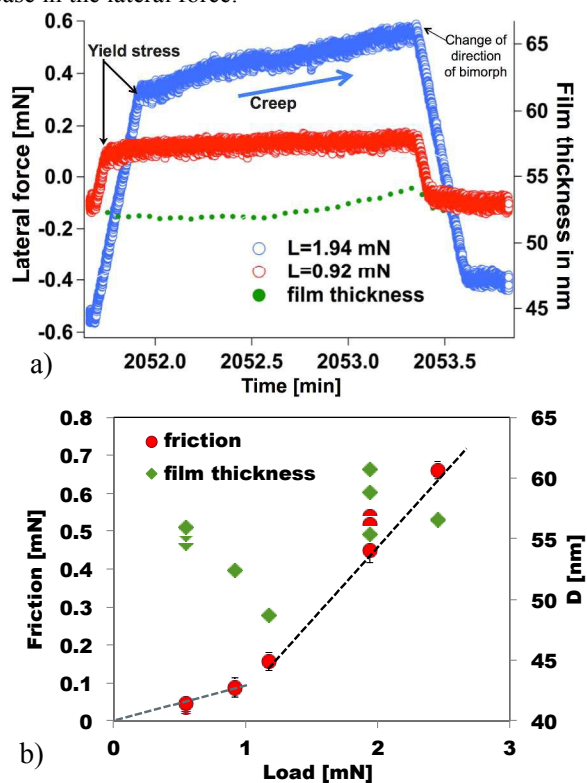

Figure 8: a) Lateral force vs. time during reciprocating sliding at 0.1 µm/s of the two mica surfaces in dry [HMIM] EtSO4 at two loads, 0.92 and 1.94 mN. The yield points are indicated with black arrows: yield strength increases with load. The figure also shows the film thickness D (right Y-axis). b) Friction vs. normal load at constant 0.1 µm/s sliding speed and 10 µm sliding distance (left Y-axis), and film thickness measured by interferometry with an accuracy of 30 pm (right Y-axis). All measurements performed in a dry N2 atmosphere.

Figure 8b shows the increase in friction with applied normal load, and the corresponding thickness of the nanoconfined IL. The IL-film that remains in the contact upon shear is roughly one order of magnitude thicker than for other ILs (D =50-60 nm) and is not squeezed out as the normal load is increased. Figure 9 shows the time-dependent film thickness upon compression between friction measurements: initially a load of 1.9 mN was applied, the friction force measured and then the surfaces were further approached, i.e. a higher load was applied. The hard-wall of the nanoconfined IL extends up to *~60 nm*

from the surface although the applied load is lower than in normal force measurements. Moreover, the characteristic transitions with dilation are also observed after a friction test, but the size of the film-thickness transition is much larger (see the labels "squeezed-out" and "dilation" in Figure 9). Both observations are in agreement with enhanced solid-like behavior upon shear, as reported for straight-chain and branched hydrocarbons.[66] The refractive index is shown in the same diagram to demonstrate there is no artefact in the interferometric measurement.
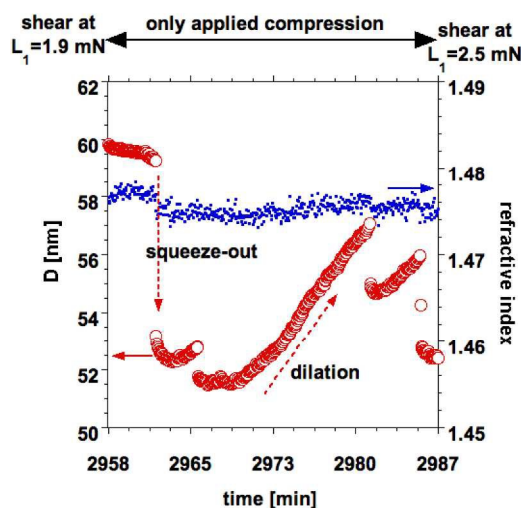

Figure 9: Time dependence of the film-thickness transitions in dry N_2 after a friction test at an applied load of 1.9 nN: upon further confinement (increasing load), a two-step transition is identified: rapid squeezing-out of layers, followed by slow dilation. The size of the transitions is significantly larger than in experiments where only normal load is applied (no shear).

Wide-Angle X-Ray scattering

X-Ray scattering studies[67] have shown that 1-alkyl-3-methyl-imidazolium ILs can form nanostructures yielding three structure-factor [$S(q)$] reflections in the q range of 2-20 nm^{-1}, corresponding to spatial correlation lengths (*d*) between 3.15 to 0.314 nm, which strongly depend on both the length of the alkyl chain and the anion[68]. Recently, Hettige and co-workers[69] reported a careful analysis of the molecular-scale origin of these three peaks often observed in ILs: the lowest q reflection is a description of the average lateral separation between IL filaments (or columnar structures of IL bundles) in a disordered continuous network, the mid q reflects the longitudinal distance between alkyl tails along a IL filament, and the higher q arises due to the average distance between charges within the IL filament (c.f. schematics in Fig. 10). In addition, the same authors performed a deconvolution of $S(q)$ into different pair correlation functions; in cases where there is the same spacing but a different phase, a negative $S(q)$ or an "anti-peak" can be observed.[70] This helps to interpret the IL scattering as it separates cation-cation, cation-anion and solvophobic interactions. The peak at low q in ILs indicates that bulk order can be propagated

over great distances, often in the form of a disordered bicontinuous or sponge-like structure where the ions form a network of alternating polar and non-polar domains due to electrostatic and solvophobic clustering.[71]

We have compared the nanostructure of [HMIM] EtSO$_4$ in bulk with that of [EMIM] EtSO$_4$ to determine the influence of the alkyl chain length, and with that of [HMIM] Ntf2 to identify the influence of the anion on the nanostructure. According to our WAXS measurements (Figure 10), the first peak for [HMIM] EtSO$_4$ (blue line) and for [HMIM] Ntf2 (red line), (both with the same cation) indicates a *d*-spacing of 1.7 nm and of 1.6 nm, respectively, confirming a disordered sponge-like phase.[72, 73] The correlation length is consistent with the distance between two similarly charged ionic moieties separated by their alkyl chains. We observe that this reflection is very broad or possibly absent for [EMIM] EtSO$_4$ (black line), in agreement with previous results.[68] This fact could be because of the shorter alkyl chain reducing the solvophobic and van der Waals driving force for segregation of polar and non-polar domains[74] or it can simply be an effect of perfect $S(q)$ peak-antipeak cancellations.[69] In fact, the three peaks have been previously detected, for quaternary trialkylmethylammonium aprotic ILs containing the NTf2 anion.[68]
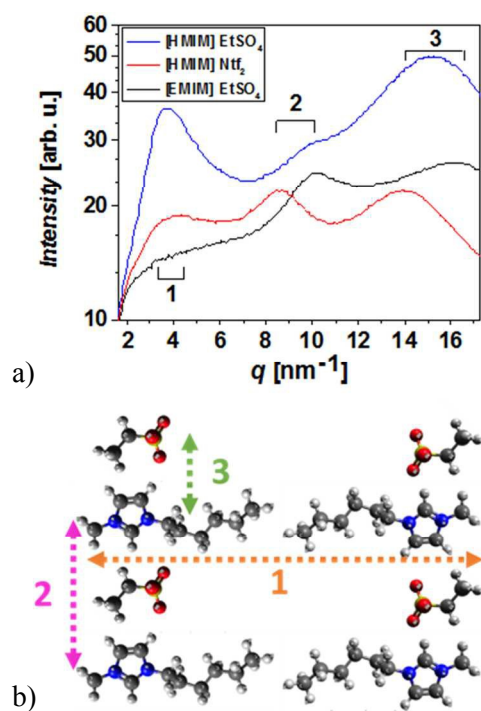

Figure 10: a) WAXS obtained for dry [HMIM] EtSO$_4$ (blue line), [HMIM] Ntf2 (red line) and [EMIM] EtSO$_4$ (black line) ILs. Reflections at the q ranges of ~4, 9, and 15 nm^{-1} (marked by 1, 2, 3) correspond to ordering of the ILs with correlation lengths of 1.6, 0.7, and 0.42 nm, respectively. The first WAXS peak is clearly more intense and narrow for [HMIM] EtSO$_4$ indicating a higher degree of order in this IL, even in the bulk state. b) Schematic of the correlation distances.

We observe that the second and third reflections for the same anion species ILs (black and blue line) are roughly positioned at the same *q*, indicating that the alkyl chains and the charges

along a IL filament are roughly at the same separation. However, for a different anion ([Ntf$_2$] red line) the alkyl chains (second peak) and the charges (third peak) are at slightly larger separation (lower *q*), while the distance between IL filaments (first peak) is not affected. Notably, the first peak arising from [HMIM] EtSO$_4$ is considerably more intense and twice as narrow compared to that obtained for [HMIM] Ntf2. Domain size is inversely proportional to the full width at half max (FWHM) of the WAXS line (Figure S5 in ESI). In other words, the ordered domains of [HMIM] EtSO$_4$ are twice as large as those observed for [HMIM] Ntf2. Taking into account that both ILs have the same cationic alkyl chain and that the first peak is a description of the average separation between IL filaments (c.f. bottom schematics in Fig. 10), it is less likely that $S(q)$ cancellations explain this behavior and we postulate that this is an indication that [HMIM] EtSO$_4$ is capable of displaying a higher degree of order—even in the absence of nanoconfinement.

Discussion

Reported force isotherms for confined ILs *typically* consist of a *short-range repulsive force* with a series of superposed steps that arise as IL-layers are squeezed out from the contact. The layer size corresponds approximately to the characteristic size of the ion pair and the order propagates to less than ~5 nm from the liquid-solid interface. In contrast, the force measurements for [HMIM] EtSO$_4$ reveal film-thickness transitions that extend up to ~ 60 nm, with sizes greater than the individual ion-pair size (~$V_m^{1/3}$=0.75 nm, where V_m is the molecular volume). Hence, these measurements provide evidence for a *longer-range order* of this IL in nanoconfinement.

The measured surface forces are reminiscent of the long-range oscillatory forces characteristic of liquid crystals (LCs).[75-79] Thus, we employed the contact-mechanics model derived by Richetti and co-workers (Figure S4a) to obtain the compressibility modulus of LCs.[78,79] This model describes the elastic force during compression of a film as a function of its elastic modulus B, the number of layers at the contact n_0 and the thickness of these layers Δ:

$$\frac{F}{R} = \frac{\pi B (D - n_0\Delta)^2}{n_0\Delta}$$

The equation was fitted to the experimentally measured force isotherms between film-thickness transitions (see an example in Figure S4b). Each parabola shows the fit for a specific number of layers, n_0. The obtained elastic modulus B for two sets of mica surfaces is shown in Figure 11. The symbols correspond to individual force-separation curves, from which the moduli were obtained.

The elastic modulus of the IL-film increases upon increasing compression—indicating "strengthening" of the IL film—and reaches values on the order of GPa, i.e. two orders of magnitude higher than the modulus of typical LCs. Although a more complex model based on thin-coating contact mechanics taking into account substrate effects and the complex contact geometry discussed before would be more appropriate, this approxima-

tion is sufficient to highlight the significant strengthening of [HMIM] $EtSO_4$ upon compression. Furthermore, these results support the idea that the increase in friction during slip (Figure 8a) results from creep, or hardening plasticity of the confined structured IL-film. Such friction measurements were performed at various loads (and speeds) and creep was observed above a load of ~0.8 mN. The change of the slope in the load-dependent friction curve (Fig. 7b) occurs at the onset of creep.
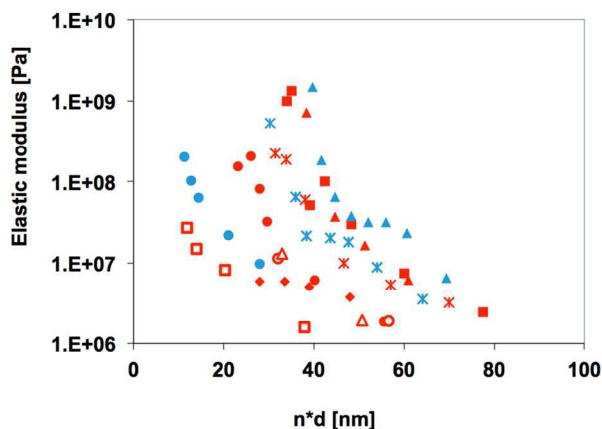

Figure 11: Elastic modulus of the dry [HMIM] $EtSO_4$ as a function of the film thickness in dry N_2 for two sets of mica surfaces (in different colours). Upon consecutive approaches (from left to right), the thickness of the IL-film increases (see different symbols for different force isotherms). Higher elastic moduli are obtained with increasing compression.

In agreement with previous findings for [HMIM] cations (with other anions[51,54]) no mesophase was observed for bulk [HMIM] $EtSO_4$ in the WAXS pattern but rather an "intermediate" order with a d-spacing~1.7 nm. The peak at ~4 nm^{-1} is broad and therefore indicates the presence of defects, i.e. a polydisperse d-spacing. The persistence of the repeating unit is larger for [HMIM] $EtSO_4$ than for the other investigated ILs. These features differ from those that are characteristic of bulk ILCs.[52] However, it is noteworthy that applied pressure (as in our force measurements) may modify the mesophorphism of ILs.[51]

It has been proposed that the layered structure resolved in force measurements results from a sponge-to-lamellar transition at the solid-liquid interface and under nanoconfinement[39], similar to that observed in surfactants and other lyotropic liquid crystals.[80] However, this sponge-to-lamellar transition confined in a symmetric system (as in the SFA experiments) had an overall attractive force, whereas the force was repulsive only in asymmetric systems.[22, 45] In both AFM and SFA force measurements, we only observed an overall net repulsive force, which is seemingly in contradiction with a sponge-to-lamellar transition occurring in the SFA experiments.

Several studies have reported the melting point depression of 1,3-dialkylimidazolium-based ILs confined to nanospaces, as determined by differential scanning thermal calorimetry.[81, 82] In contrast, Chen et. al.[50] identified the transition of [BMIM] PF_6 from a liquid to a high-melting-point crystal via selected-area electron diffraction and x-ray diffraction, when confined within multi-walled carbon nanotubes (MWCNTs) with an inner di-

ameter of 5-10 nm, which is also supported by theory.[83] Since the estimated elastic modulus of the IL-film reaches values on the order of GPa, we propose that the confinement upon applied pressure in our force measurements induces a long-range liquid-to-solid phase change of [HMIM] $EtSO_4$ in nanoconfinement that has not been observed for other imidazolium ILs in similar force measurements. Apparently this IL is more prone to "ordering" than the other investigated ILs, as indicated by the WAXS measurements.

It should also be mentioned that AFM measurements performed with a sharp tip (radius ~ 4nm), i.e. in the absence of confinement, show only short-range order, as is the case for other ILs (see Figure S6 in ESI). Two film-thickness transitions were observed, the largest being ~1.2 nm, prior to the hard wall. The layer thickness (~1.2 nm) suggests a self-assembled bilayer structure at the IL-solid interface, consistent with previous SFA measurements for other ionic liquids with long alkyl chains ([HMIM] Ntf2),[36] and also with our WAXS results (see peak at low q). These results demonstrate that nanoconfinement is required for long-range order to develop in dry [HMIM] $EtSO_4$.

Summarizing, our results indicate that nanoconfinement promotes a phase transformation of dry [HMIM] $EtSO_4$ into a *long-range, solid-like or solid structure* that differs from the *short-range,* solid-like structures previously reported for other ILs. Shear measurements are consistent with the formation of a solid in confinement that undergoes creep owing to the presence of defects. The AFM force measurements support the irreversibility of the phase transition upon removal of the nanoconfinement.

Owing to the hygroscopic behaviour of the IL and the exposure to ambient air at the beginning of the experiment, we cannot exclude traces of water being present in the force measurements. Drying of residual water could have an influence on the results, as previously reported.[20, 30, 31] Traces of water in the IL are also expected in the colloidal-probe AFM experiments. AFM experiments extend over a few hours, whereas SFA experiments extend over days, and therefore the IL is subjected to much longer drying times in the SFA measurements. However, the observed changes in the force-separation curves are qualitatively similar, indicating that if drying of water traces were to have occurred during the measurements in dry N_2, it would not have been relevant, as far as the observed phenomena were concerned. A systematic study of the influence of the water uptake on the structure of nanoconfined [HMIM] $EtSO_4$ is ongoing.

Conclusions

We have investigated the properties of nanoconfined and bulk [HMIM] $EtSO_4$ under dry conditions by means of SFA, colloidal-probe AFM measurements, and WAXS. Repeatedly applied nanoconfinement of [HMIM] $EtSO_4$ between mica surfaces can induce *a long-range* liquid-to-solid transition of the IL that apparently remains after confinement has been removed. The solid-like IL has a pronounced layered structure, and the layer size exceeds the size of the ion pair. The nanoconfined IL ap-

pears to strengthen upon applied pressure, and the estimated elastic modulus increases to GPa values. The thickness of the IL-film is about ten times larger than that of other ILs confined at similar pressures. In addition, WAXS has shown a more pronounced bulk order compared to other ILs with the same cation or anion, suggesting that the combination of [HMIM] as cation, and EtSO$_4$ as anion, and the corresponding interactions, lead to this particular behavior.

The presented results suggest that a complex phase-transition behavior exists for nanoconfined ILs. Our results show that long-range ordering, and confinement-induced phase transitions can be tuned through tailored ion pairing. However, many questions still remain – what roles do substrate chemistry and charge play in phase-transition and ordering behavior? Under what conditions can spontaneous solidification occur? What are the thermal and electrochemical stabilities of the new phase? Could such a solid phase act as a solid-state lubricant and as an electrolyte in a supercapacitor? The implications of these findings are of significance with respect to IL applications in many areas, including lubrication and energy-storage systems.

Materials and Experimental Methods

Materials

1-hexyl-3-methyl-imidazolium ethyl sulphate, [HMIM] EtSO$_4$ (Iolitec, Heilbronn, Germany), purity >98%, water content <100 ppm is hygroscopic, owing to significant water-anion hydrogen-bonding (see optimized ion geometry in Figure S7a in the Electronic Supplementary Information, ESI). Melting point and glass-transition temperatures are below -50ºC, as obtained by differential scanning calorimetric analysis (DSC-8000, Perkin Elmer, USA). The X-ray photoelectron survey spectrum of the dry IL deposited on mica after 18 h in vacuum is shown in Figure S8 in the ESI.

Extended Surface Forces Apparatus

An extended surface forces apparatus (eSFA)[59, 84] was used to explore normal and friction forces between mica surfaces across the selected IL. The SFA is an instrument that directly measures forces occurring between two mica surfaces. A central element of this method is the optical measurement of the distance between the surfaces D based on interferometry[85, 86]. The two surfaces are cylindrically shaped (R=20mm), by virtue of being glued to cylindrical glass supports and facing each other such that the cylinder axes cross at an angle of 90°. One surface is supported by a spring and is approached towards the other using an approach actuator, whose position is known over time. If there is a surface force, this spring deflects, and the normal surface force F results from the distance measurement with known spring constant k_n (1940±60 N/m and 526 N/m were used in this work, see schematics in Figure S7b). The two transparent mica layers form an optical thin-film interferometer. The rear of each mica layer is coated with a semi-transparent silver mirror, in order to improve the reflectivity. White light is

directed through the interferometer and analyzed in an imaging spectrograph.

A number of improvements in accuracy, resolution, speed, mechanical drift, thermal stability and imaging have been made to the instrument, and for this reason it is referred to as the "extended Surface Force Apparatus" (eSFA). The upgrades are all described in detail in the literature[59, 87]. Thus, the transmitted interference spectrum consists of fringes of equal chromatic order (FECO), which are analysed by a numerical, fast-spectral-correlation algorithm, to determine both the distance D between the surfaces at the point of closest approach (PCA) with a standard deviation of better than 30 pm over a distance ranging from 0 to 10 μm, and the refractive index of the medium. It is important to note that while changes in film thickness at a given force (called film-thickness transitions of size Δ) are detected at full precision, the absolute accuracy of distance measurement D (e.g. absolute zero) at high compression is inferior[58]; an error in D smaller than 1 nm has been estimated at F/R=250 mN/m (unpublished results). The simplified disposition of the optical elements in the eSFA minimizes human influence and allows the adjustment of the PCA to better than 1 μm laterally in an automated fashion.

Force-separation curves were measured under dry conditions by approaching/separating the surfaces at constant speed (0.2 nm/s to 1 nm/s) on 12 different pairs of mica surfaces, collecting more than 200 force-distance isotherms. For the friction experiments, the lower surface was moved laterally at 0.1 μm/s by means of a piezoelectric bimorph crystal, reciprocating with an amplitude of 10 μm. The bimorph was mounted on a spring with a spring constant k_n=526 N/m.

The shear forces acting on the upper surface were measured with a strain gauge mounted on a spring[88] (k_f = 2300±100 N/m) at a measuring rate of 300 Hz, while the surface separation was simultaneously measured by multiple-beam interferometry.

Thin mica sheets were prepared by manually cleaving ruby mica of optical quality Grade #1 (S&J Trading, Inc. NY, USA) in a class-100 laminar-flow cabinet. Uniformly thick (2–5.5 μm) mica sheets of size ~8 mm x 8 mm were cut using surgical scissors, to avoid possible contamination with nanoparticles[89]. A 40 nm thick silver film was thermally evaporated onto mica sheets in vacuum (2·10^{-6} mbar). The silver-coated mica sheets were glued onto cylindrical lenses using resin glue (EPON 1004F). The samples were then immediately inserted into the sealed eSFA, the fluid cell purged with dry N$_2$, and the mica thickness determined by means of thin-film interferometry in mica-mica contact.

After that, a 20 μl-droplet of vacuum-dried IL was deposited between the mica surfaces using a Hamilton syringe with a flat-end needle (Model 710), during continuous purging of the eSFA cell with dry N$_2$. The IL was exposed to laboratory air for a maximum of 2 minutes, during which water uptake could take place. Thus, removal of some residual water during equilibration in dry N$_2$ in the eSFA cannot be excluded. The cell was sealed and the system left to equilibrate for at least 3 hours. Measurements were performed at 22±0.1 ºC.

Colloidal Probe Atomic Force Microscopy

Colloidal-probe AFM measurements were acquired with an Asylum MFP3D AFM (Santa Barbara, CA, USA) and with an Asylum Cypher AFM (Santa Barbara, CA, USA), both in contact mode. Gold coated, tipless, AFM cantilevers (Mikromasch, Tallinn, Estonia) were used in this study. The spring constant of the AFM cantilever was determined according to the thermal-noise method.[90] A 40 µm diameter colloidal probe (Corpuscular, Cold Spring, NY, USA) was glued to the end of the cantilever with NOA 63 optical adhesive (Norland, Cranberry, NJ, USA). The AFM colloidal probe tip was rinsed by immersing it in acetone for two hours, followed by isopropanol, and ethanol rinsing. Immediately before experiments the tip was treated in a UV-Ozone cleaner for 20 minutes. The AFM chambers were continuously purged with dry N_2.

Normal force-separation curves were obtained at constant approach speeds of 15-30 nm/s with the MFP3D AFM in dry N_2 atmosphere (RH<5%) at 27 ± 2 ºC. The spring constant of the experiments reported here was 0.07 N/m and the maximum applied force was 10 nN. A 25 µL droplet of dry [HMIM] $EtSO_4$ was placed on a freshly cleaved mica surface. During the transfer, the droplet was exposed to ambient laboratory air (~40 % RH) for approximately two minutes, which might lead to traces of water being taken up by the IL.

The force measurements on the two separate mica pieces were acquired with the Cypher AFM in a dry N_2 atmosphere (RH<2%) at 27 ± 2 ºC. A 20 µL droplet of dry [HMIM] $EtSO_4$ was placed on the first piece of freshly cleaved mica. During the transfer, the droplet was exposed to ambient laboratory air (~14% RH) for approximately two minutes, which might lead to traces of water being taken up by the IL, as well. The colloidal AFM probe was then disengaged and the first mica-IL sample was removed from the chamber. A dry 20 µL droplet of [HMIM] $EtSO_4$ was placed on a second piece of freshly cleaved mica from the same batch as the first piece. The colloidal probe remained in the tip holder during placement of the second mica sample. Force-separation curves were obtained at approach speeds of 10 nm/s with the Cypher AFM. The spring constant of the experiments reported here was 0.2 N/m and the maximum applied force was 30 nN.

The entire sequence of force measurements on a single mica substrate was collected within 2 hours.

Wide-Angle X-ray Scattering (WAXS)

Dry ILs were transferred into 1.5 mm quartz X-ray capillaries (Hilgenberg Glas, Germany) in a glove box that was purged with N_2, and the capillaries were sealed with epoxy adhesive. The WAXS experiments were conducted in home-built (with the support of Forvis Technologies, Santa Barbara) equipment composed of a Xenocs GeniX3D CuK$_\alpha$ Ultra Low Divergence X-ray source (1.54Å / 8 keV), with a divergence of ~ 1.3 mrad. The sample-to-detector distance was 175.7 mm, yielding a q range of 0.86 nm^{-1} to 17.36 nm^{-1} (corresponding to 7.3–0.36 nm in real space). The 2D-diffraction data were radially averaged upon acquisition on a Pilatus 300K 20 Hz hybrid pixel Detector (Dectris) and integrated using FIT2D software: (http://www.esrf.eu/computing/scientific/FIT2D) from ESRF.

Notes and references

[a]Lab. for Surface Science and Technology, Dept. of Materials, ETH Zurich, CH-8093 Zurich, Switzerland
[b]Dept. of Civil and Environmental Engineering, University of Illinois at Urbana-Champaign, IL-61801 Urbana, USA
[c]Dept. of Materials Science and Engineering, University of Illinois at Urbana-Champaign, IL-61801 Urbana, USA
[d]Dipartimento di Scienze Chimiche e Geologiche, Università di Cagliari, 09042 Cagliari, Italy.

1. M. Armand, F. Endres, D. R. MacFarlane, H. Ohno and B. Scrosati, *Nat Mater*, 2009, **8**, 621-629.
2. H. T. Liu, Y. Liu and J. H. Li, *Physical Chemistry Chemical Physics*, 2010, **12**, 1685-1697.
3. H. Weingaertner, *Angew Chem Int Edit*, 2008, **47**, 654-670.
4. T. L. Greaves and C. J. Drummond, *Chemical Society Reviews*, 2008, **37**, 1709-1726.
5. C. F. Ye, W. M. Liu, Y. X. Chen and L. G. Yu, *Chem Commun*, 2001, 2244-2245.
6. M. Palacio and B. Bhushan, *Tribol Lett*, 2010, **40**, 247-268.
7. M. Palacio and B. Bhushan, *Journal of Vacuum Science & Technology A: Vacuum, Surfaces, and Films*, 2009, **27**, 986.
8. J. J. Nainaparampil, B. S. Phillips, K. C. Eapen and J. S. Zabinski, *Nanotechnology*, 2005, **16**, 2474-2481.
9. B. Bhushan, M. Palacio and B. Kinzig, *Journal of colloid and interface science*, 2008, **317**, 275-287.
10. W. Zhao, Y. Wang, L. Wang, M. Bai and Q. Xue, *Colloids and Surfaces A: Physicochemical and Engineering Aspects*, 2010, **361**, 118-125.
11. I. Minami, *Molecules*, 2009, **14**, 2286-2305.
12. M. D. Bermudez, A. E. Jimenez, J. Sanes and F. J. Carrion, *Molecules*, 2009, **14**, 2888-2908.
13. M. Mezger, H. Schroder, H. Reichert, S. Schramm, J. S. Okasinski, S. Schoder, V. Honkimaki, M. Deutsch, B. M. Ocko, J. Ralston, M. Rohwerder, M. Stratmann and H. Dosch, *Science*, 2008, **322**, 424-428.
14. Y. Lauw, M. D. Horne, T. Rodopoulos, V. Lockett, B. Akgun, W. A. Hamilton and A. R. J. Nelson, *Langmuir*, 2012, **28**, 7374-7381.
15. B. Fitchett and J. Conboy, *The journal of physical chemistry. B*, 2004, **108**, 20255-20262.
16. T. Cremer, M. Cremer, A. Stark, H. P. Deyko and Maier, *Langmuir*, 2011, **27**, 3662-3671.
17. B. Uhl, T. Cremer, M. Roos, F. Maier, H. P. Steinruck and J. Behm, *Physical Chemistry Chemical Physics*, 2013, **15**, 17295-17302.
18. T. Cremer, C. Kolbeck, K. R. J. Lovelock, N. Paape, R. Wolfel, P. S. Schulz, P. Wasserscheid, H. Weber, J. Thar, B. Kirchner, F. Maier and H. P. Steinruck, *Chem-Eur J*, 2010, **16**, 9018-9033.

19.   A. Deyko, T. Cremer, F. Rietzler, S. Perkin, L. Crowhurst, T. Welton, H. P. Steinruck and F. Maier, *J Phys Chem C*, 2013, **117**, 5101-5111.
20.   A. Arcifa, A. Rossi, R. M. Espinosa-Marzal and N. D. Spencer, *The Journal of Physical Chemistry C*, 2014, **118**, 29389-29400.
21.   H. Li, M. W. Rutland and R. Atkin, *Phys Chem Chem Phys*, 2013, **15**, 14616-14623.
22.   H. Li, F. Endres and R. Atkin, *Phys Chem Chem Phys*, 2013, **15**, 14624-14633.
23.   X. Zhang, Y. X. Zhong, J. W. Yan, Y. Z. Su, M. Zhang and B. W. Mao, *Chem Commun*, 2012, **48**, 582-584.
24.   R. Köhler, J. Restolho, R. Krastev, K. Shimizu, J. N. Canongia Lopes and B. Saramago, *The Journal of Physical Chemistry Letters*, 2011, **2**, 1551-1555.
25.   O. Werzer and R. Atkin, *Physical Chemistry Chemical Physics*, 2011, **13**, 13479-13485.
26.   Y. Yokota, T. Harada and K.-i. Fukui, *Chem Commun*, 2010, **46**, 8627-8629.
27.   S. Bovio, A. Podestà, C. Lenardi and P. Milani, *The Journal of Physical Chemistry B*, 2009, **113**, 6600-6603.
28.   R. Atkin and G. G. Warr, *The Journal of Physical Chemistry C*, 2007, **111**, 5162-5168.
29.   Y. Liu, Y. Zhang, G. Wu and J. Hu, *J Am Chem Soc*, 2006, **128**, 7456-7457.
30.   R. M. Espinosa-Marzal, A. Arcifa, A. Rossi and N. D. Spencer, *The Journal of Physical Chemistry Letters*, 2014, **5**, 179–184.
31.   R. M. Espinosa-Marzal, A. Arcifa, A. Rossi and N. D. Spencer, *J Phys Chem C*, 2014, **118**, 6491−6503.
32.   M. A. Gebbie, M. Valtiner, X. Banquy, E. T. Fox, W. A. Henderson and J. N. Israelachvili, *P Natl Acad Sci USA*, 2013, **110**, 9674-9679.
33.   A. M. Smith, K. R. J. Lovelock, N. N. Gosvami, P. Licence, A. Dolan, T. Welton and S. Perkin, *J Phys Chem Lett*, 2013, **4**, 378-382.
34.   A. M. Smith, K. R. J. Lovelock, N. N. Gosvami, T. Welton and S. Perkin, *Physical Chemistry Chemical Physics*, 2013, **15**, 15317-15320.
35.   S. Perkin, *Physical Chemistry Chemical Physics*, 2012, **14**, 5052-5062.
36.   S. Perkin, L. Crowhurst, H. Niedermeyer, T. Welton, A. M. Smith and N. N. Gosvami, *Chemical Communications*, 2011, **47**, 6572-6574.
37.   S. Perkin, T. Albrecht and J. Klein, *Physical Chemistry Chemical Physics*, 2010, **12**, 1243-1247.
38.   R. G. Horn, D. F. Evans and B. W. Ninham, *J Phys Chem-Us*, 1988, **92**, 3531-3537.
39.   T. Carstens, R. Hayes, S. Z. El Abedin, B. Corr, G. B. Webber, N. Borisenko, R. Atkin and F. Endres, *Electrochimica Acta*, 2012, **82**, 48-59.
40.   M. A. Gebbie, M. Valtiner, X. Banquy, W. A. Henderson and J. N. Israelachvili, *Proceedings of the National Academy of Sciences*, 2013, **110**, E4122.
41.   A. A. Lee, D. Vella, S. Perkin and A. Goriely, *The Journal of Physical Chemistry Letters*, 2014.
42.   S. Perkin, M. Salanne, P. Madden and R. Lynden-Bell, *Proceedings of the National Academy of Sciences*, 2013, **110**, E4121.
43.   N. Nanbu, Y. Sasaki and F. Kitamura, *Electrochem Commun*, 2003, **5**, 383-387.
44.   M. Sha, G. Wu, H. Fang, G. Zhu and Y. Liu, *The Journal of Physical Chemistry C*, 2008, **112**, 18584-18587.
45.   R. Hayes, G. G. Warr and R. Atkin, *Physical Chemistry Chemical Physics*, 2010, **12**, 1709-1723.
46.   C. Fredlake, J. Crosthwaite, D. Hert, S. N. V. K. Aki and J. Brennecke, *Journal of Chemical & Engineering Data*, 2004, **49**, 954-964.
47.   A. Fernandez, J. S. Torrecilla, J. García and F. Rodríguez, *Journal of Chemical & Engineering Data*, 2007, **52**, 1979-1983.
48.   Y. Shimizu, Y. Ohte, Y. Yamamura, K. Saito and T. Atake, *The journal of physical chemistry. B*, 2006, **110**, 13970-13975.
49.   H. Shirota, T. Shirota, H. Mandai, T. Fukazawa and Kato, *Journal of Chemical & Engineering Data*, 2011, **56**, 2453-2459.
50.   S. Chen, G. Wu, M. Sha and S. Huang, *J Am Chem Soc*, 2007, **129**, 2416-2417.
51.   K. Binnemans, *Chem Rev*, 2005, **105**, 4148-4204.
52.   J. De Roche, C. M. Gordon, C. T. Imrie, M. D. Ingram, A. R. Kennedy, F. Lo Celso and A. Triolo, *Chem Mater*, 2003, **15**, 3089-3097.
53.   O. Russina, A. Triolo, L. Gontrani and R. Caminiti, *The Journal of Physical Chemistry Letters*, 2011, **3**, 27-33.
54.   A. E. Bradley, C. Hardacre, J. D. Holbrey, S. Johnston, S. E. J. McMath and M. Nieuwenhuyzen, *Chem Mater*, 2002, **14**, 629-635.
55.   D. W. Bruce, S. Estdale, D. Guillon and B. Heinrich, *Liq Cryst*, 1995, **19**, 301-305.
56.   M. P. Singh, R. K. Singh and S. Chandra, *Progress in Materials Science*, 2014, **64**, 73-120.
57.   J. N. Israelachvili, *Intermolecular and Surface Forces: Revised Third Edition*, Elsevier Science, 2011.
58.   R. M. Espinosa-Marzal, T. Drobek, T. Balmer and M. P. Heuberger, *Physical Chemistry Chemical Physics*, 2012, **14**, 6085-6093.
59.   M. Heuberger, *Review of Scientific Instruments*, 2001, **72**, 1700-1707.
60.   J. Sweeney, G. B. Webber, M. W. Rutland and R. Atkin, *Physical Chemistry Chemical Physics*, 2014, **16**, 16651-16658.
61.   P. M. McGuiggan, J. Zhang and S. M. Hsu, *Tribology Letters*, 2001, **10**, 217-223.
62.   Y. Yang, J. Singh and M. Ruths, *Rsc Adv*, 2014, **4**, 18801-18810.
63.   Y. Lei and Y. Leng, *Phys Rev Lett*, 2011, **107**, 47801-47805.
64.   R. M. Pashley, *Journal of Colloid and Interface Science*, 1981, **83**, 531-546.
65.   O. Y. Fajardo, F. Bresme, A. A. Kornyshev and M. Urbakh, *Sci. Rep.*, 2015, **5**.
66.   M. L. Gee, P. M. Mcguiggan, J. N. Israelachvili and A. M. Homola, *Journal of Chemical Physics*, 1990, **93**, 1895-1906.
67.   W. Zheng, A. Mohammed, L. G. Hines, Jr., D. Xiao, O. J. Martinez, R. A. Bartsch, S. L. Simon, O. Russina, A. Triolo and E. L. Quitevis, *J Phys Chem B*, 2011, **115**, 6572-6584.
68.   O. Russina, L. Gontrani, B. Fazio, D. Lombardo, A. Triolo and R. Caminiti, *Chemical Physics Letters*, 2010, **493**, 259-262.
69.   J. J. Hettige, J. C. Araque and C. J. Margulis, *J. Phys. Chem. B*, 2014, **118**, 12706−12716.
70.   H. K. Kashyap, J. J. Hettige, H. V. R. Annapureddy and C. J. Margulis, *Chem. Commun.*, 2012, **48**, 5103–5105.
71.   R. Hayes, S. Imberti, G. G. Warr and R. Atkin, *Physical Chemistry Chemical Physics*, 2011, **13**, 13544-13551.
72.   Y. Shen, T. L. Greaves, D. F. Kennedy, A. Weerawardena, N. Kirby, G. H. Song and C. J. Drummond, *Phys Chem Chem Phys*, 2014, **16**, 21321-21329.
73.   T. L. Greaves, D. F. Kennedy, S. T. Mudie and C. J. Drummond, *J Phys Chem B*, 2010, **114**, 10022-10031.
74.   T. L. Greaves and C. J. Drummond, *Chemical Society Reviews*, 2013, **42**, 1096-1120.
75.   M. Ruths and S. Granick, *Langmuir*, 2000, **16**, 8368-8376.
76.   M. Ruths, M. Heuberger, V. Scheumann, J. J. Hu and W. Knoll, *Langmuir*, 2001, **17**, 6213-6219.
77.   M. Ruths, S. Steinberg and J. N. Israelachvili, *Langmuir*, 1996, **12**, 6637-6650.
78.   P. Richetti, P. Kekicheff and P. Barois, *J Phys Ii*, 1995, **5**, 1129-1154.
79.   G. Carbone, B. Zappone, R. Barberi, R. Bartolino and I. Musevic, *Physical Review E*, 2011, **83**.
80.   D. A. Antelmi, P. K√©kicheff and P. Richetti, *Langmuir*, 1999, **15**, 7774-7788.
81.   M. Kanakubo, Y. Hiejima, K. Minami, T. Aizawa and H. Nanjo, *Chem Commun*, 2006, 1828-1830.
82.   M. A. Neouze, J. Le Bideau, P. Gaveau, S. Bellayer and A. Vioux, *Chem Mater*, 2006, **18**, 3931-3936.
83.   K. Dong, G. Zhou, X. Liu, X. Yao, S. Zhang and A. Lyubartsev, *The Journal of Physical Chemistry C*, 2009, **113**, 10013-10020.
84.   J. N. Israelachvili, *Journal of Colloid and Interface Science*, 1973, **44**, 259-272.

85. J. N. Israelachvili and D. Tabor, *Proceedings of the Royal Society of London. A. Mathematical and Physical Sciences*, 1972, **331**, 19-38.
86. D. Tabor and R. H. S. Winterton, *Proceedings of the Royal Society of London. Series A, Mathematical and Physical Sciences*, 1969, **312**, 435-450.
87. M. Heuberger, J. Vanicek and M. Zäch, *Review of Scientific Instruments*, 2001, **72**, 3556-3560.
88. G. Luengo, F. J. Schmitt, R. Hill and J. Israelachvili, *Macromolecules*, 1997, **30**, 2482-2494.
89. M. Heuberger and M. Zäch, *Langmuir*, 2003, **19**, 1943-1947.
90. J. L. Hutter and J. Bechhoefer, *Review of Scientific Instruments*, 1993, **64**, 1868-1873.